Incident photon energy dependence of the resonant x-ray magnetic scattering cross section of a samarium film

A. Stunault,[1,2] K. Dumesnil,[3] C. Dufour,[3] C. Vettier,[2,*] and N. Bernhoeft[4]
[1]*XMaS, the UK CRG at European Synchrotron Radiation Facility, BP 220, F-38043 Grenoble Cedex, France and Department of Physics, University of Liverpool, Liverpool L69 7ZE, United Kingdom*
[2]*Institut Laue Langevin, BP 156X, F-38042 Grenoble Cedex 9, France*
[3]*Laboratoire de Physique des Matériaux, Université Henri Poincaré-Nancy 1, BP 239, 54506 Vandoeuvre les Nancy Cedex, France*
[4]*CEA/Grenoble, DRFMC/SPSMS/MRS, F-38054 Grenoble Cedex, France*
(Received 3 June 2001; published 23 January 2002)

Resonant x-ray magnetic scattering is widely used as an element selective probe of magnetism in solids. The present work deals with a different, less frequently addressed aspect: the electronic shell selectivity. Due to the complexity of the atomic effects inherent to the resonant process and at the origin of the electronic shell selectivity, the data are generally considered on a qualitative basis. Here, we try to extend the arguments to a semiquantitative level. We show, through a detailed spectroscopic study of the resonance at the L_2 and L_3 edges of samarium in a single-crystal epitaxial film, how the exploitation of the atomic effects can lead to a deeper understanding of long-range magnetic order in this material. At the $L_{2,3}$ edges of rare earths, dipole resonances carry information on the polarization of the $5d$ band, whereas quadrupole resonances reflect the polarization of the $4f$ shell. The narrow width of the $4f$ band permits the interpretation of the quadrupole resonance below the L_3 edge using atomic considerations. A systematic study of the dependence of the $4f$ quadrupole resonance on wave-vector transfer shows that, within our resolution, the magnitude of the $4f$ moments in samarium is independent of the local environment (cubic or hexagonal). On the other hand, the energy dependence of the dipole resonance at and above the L_2 and L_3 absorption edges shows two maxima and is interpreted in the framework of an extended density of $5d$ states. Finally, the relative temperature dependences of the dipole and quadrupole resonances sheds light upon the respective contributions of the $4f$ and $5d$ levels to the long-range magnetic order in samarium.

DOI: 10.1103/PhysRevB.65.064436 PACS number(s): 75.25.+z, 78.70.Ck

I. INTRODUCTION

Samarium metal constitutes an atypical case in the rare-earth series, on account of both its crystal structure and its electronic properties. The crystal structure, referred to as the ''Sm structure,'' is intermediate between the hcp structure of the heavy rare earths and the dhcp structure adopted by most of the light rare earths.[1] The Sm structure is rhombohedral, space group $R\bar{3}m$, with three atoms per unit cell. It is more simply visualized as the compact stacking of nine hexagonal (**a**,**b**) planes along **c**, with lattice constants $a=3.63$ Å and $c=26.21$ Å at room temperature. There are two structural domains organized in layers perpendicular to the **c** axis and corresponding to the two different stacking sequences, $A_cB_hA_hB_cC_hB_hC_cA_hC_h$ or $A_cC_hA_hC_cB_hC_hB_cA_hB_h$, along the **c** axis. The h and c subscripts refer to the hexagonal or cubic nearest-neighbor arrangement of the Sm sites. The structural domains have been shown to coexist with equal populations in a bulk single-crystal sample,[1] although single domain crystals also exist.[2]

Samarium undergoes transitions to two distinct antiferromagnetic structures, at $T_N{}^h=106$ K and $T_N{}^c=14$ K.[3] Owing to the important thermal neutron absorption cross section ($\approx$6000 barns for the natural element), samarium is one of the less studied rare-earth elements on a microscopic scale using the traditional tool of magnetic neutron scattering. A pioneering neutron study performed on an isotopically enriched single-crystal sample[4] has shown that, below $T_N{}^h$, only the moments associated with the hexagonal sites order. The hexagonal (**a**,**b**) planes carry time averaged moments which are ferromagnetically aligned, with their axes pointing along **c**. Neighboring hexagonal planes couple ferromagnetically, and then antiferromagnetically with the next-nearest hexagonal plane, in a $(0++0--0++0--)$ sequence, doubling the unit cell in the **c** direction, with a propagation vector (0 0 1.5) in the hexagonal cell.[4] The zeros in the plane sequence correspond to the cubic planes, where the (0 0 1.5) Fourier component of the time-averaged moments is zero. Each structural domain supports two independent magnetic antiphase domains (moment reversal). More recent resonant x-ray magnetic scattering (RXMS) results are consistent with this structure.[5] Below $T_N{}^c$, the magnetic structure of the hexagonal sublattice is unchanged, but coexists with a more complex magnetic structure on the cubic sites. The propagation vector is $(\frac{1}{4}\ 0\ \frac{1}{4})$ or $(-\frac{1}{4}\ 0\ \frac{1}{4})$ depending on the structural domain, leading to 12 magnetic domains (i.e., two magnetic antiphase domains (moment reversal) associated to each of the three in-plane axes, and this for each structural domain). The moments on the cubic sites point in the **c** direction, as on the hexagonal sites. The calculated Sm^{3+} free ion moment ($4f^5$ configuration) is $0.71\mu_B$, the small value resulting from the opposition of spin and orbital moments. The net magnetic moment on the samarium sites, deduced from the neutron-scattering study,[4] has the even smaller value of $0.1\mu_B$. A

large polarization of the conduction electrons parallel to the ionic spin has been invoked to account for this extremely reduced moment. In contrast, a recent neutron-scattering study on a 5000-Å-thick samarium film has indicated a much larger moment of $1.2 \pm 0.2 \mu_B$.[6]

Samarium, like all metallic rare earths, has a large interionic separation compared with the spatial extent of the $4f$ shell. This has been taken to imply the cooperation of conduction electron states in the formation of long-range magnetic order in an essential way.[7] The differentiation of $4f$ and $5d$ magnetism thus becomes a central issue in the understanding of the magnetic properties. Insight into the contributions of the localized $4f$ shell and the delocalized $5d$ band to the time averaged magnetic moments is traditionally gained from the study of the magnetic form factors as deduced from neutron-scattering experiments.[8] The $5d$ shell has a larger spatial extension than the $4f$ shell, and, consequently, the $5d$ form factor falls off more rapidly at higher wave-vector transfer. A relative weakness of neutron scattering is, however, the inability to measure independently the contributions of the different electronic shells to the long-range magnetic order, in a model-independent fashion. Recent experimental developments show that RXMS has this capability.[9]

RXMS is based on the enhancement of the x-ray magnetic scattering cross section close to an absorption edge.[10] At the $L_{2,3}$ absorption edges in the rare-earth metals, the resonant process involves the promotion of $2p$ core electrons to empty intermediate states in the vicinity of the Fermi level and their subsequent decay. If the core hole formed by photoelectron promotion is taken to be localized, the scattering amplitude becomes site specific and, on this assumption, single-ion models of the magnetic scattering cross section have been developed.[10] The strongest matrix elements generally derive from electric dipole ($E1$) transitions, which lift the electron to vacant states of $6s$ or $5d$ character. The $6s$ wave function oscillates more strongly in the core region than the $5d$, resulting in a smaller overlap integral with the $2p$ core level. The $(2p \rightarrow 5d \rightarrow 2p)$ dipole matrix elements are then anticipated to be substantially larger than those of the $(2p \rightarrow 6s \rightarrow 2p)$ and to give the dominant contribution to both the magnetic and nonmagnetic dipole cross sections. In addition to these dipole transitions, one anticipates contributions from the electric quadrupole matrix elements ($E2$ transitions), involving vacancies in the $4f$ density of states, to the magnetic scattering cross section. The $E2$ transitions $(2p \rightarrow 4f \rightarrow 2p)$ may also yield a significant resonant cross section, on account of the large $4f$ polarization.

Several RXMS studies have taken advantage of the *element* selectivity to separate the contributions of different elements to the magnetism in compounds,[11] solid solutions,[12–16] or superlattices.[17] The present work aims at clarifying a less frequently addressed aspect of RXMS: the *electronic shell* selectivity. Two studies have made use of this possibility.[17,18] In Nd/Pr superlattices[17] polarization of the $5d$ band of ''paramagnetic'' Pr layers is induced by the coherent long-range order in Nd through the superlattice. In $DyFe_4Al_8$,[18] one observes the polarization of the Dy $5d$ shell both under the influence of the ordered Fe sublattice at elevated temperatures and by the $4f$ moments at lower temperatures.

$E1$ and $E2$ transitions have energies that generally differ by a few eV. With an energy resolution of 1–2 eV, the RXMS method becomes electronic shell selective. In this work, we exploit this aspect of resonant scattering to study the interplay between $4f$ and $5d$ polarizations in the establishment of long-range magnetic order in samarium. The identification of the dipole or quadrupole origin of the resonance requires a careful spectroscopic study, simultaneously taking into account the energy dependence, the polarization of the incident and scattered photon beams, and the dependence of the scattered intensity on the wave vector transfer.[10] Such studies have greatly benefited from the advent of dedicated beamlines at third generation synchrotron sources: with higher flux and high degree of linear polarization, one can make an extensive use of polarization analysis of the scattered beam.[19] This method, being based on scattering at 90° by an analyzer crystal, has the further advantage of drastically reducing the parasitic fluorescence signal.

Rather extended spectroscopic studies of the resonance at the $L_{2,3}$ edges of the heavy rare earths Ho,[20] Tb,[21] Dy,[22] and Tm,[23] already exist, but generally do not show a clear separation of $E1$ and $E2$ contributions. The study of Er has proved more complicated due to multiple-scattering effects.[24] The study of the resonance in the light rare earths is more difficult, primarily on account of the weak intensities. For example, published RXMS work on Nd only makes use of the resonant enhancement to investigate the complex magnetic structure.[25] Previously reported resonances in Sm are of very low intensity.[5,26] Our preliminary study of a samarium epitaxial film[9,27] revealed three well defined resonances in the magnetic scattering signal around the L_3 absorption edge [Fig. 1(a)]. Through simple qualitative considerations we could attribute the two high-energy resonances to $E1$ transitions to the $5d$ band, while the third one below the edge was assigned to $E2$ transitions to the $4f$ shell. At the L_2 edge, the same study[9] shows negligible quadrupole resonance and a double dipole resonance [Fig. 1(b)]. This complicated energy dependence is not fully accounted for by the existing theory, based on atomic considerations.[10] In the following we extend the above qualitative analysis to a more quantitative one, based on the itinerant antiferromagnetic state, wherein: (i) the $E2$ resonance, strikingly large in samarium compared to other rare earths,[20–25] is shown to fit the predictions from the narrow-band limit (atomic theory) and (ii) a broadband model[28] is used to interpret the observed energy line shape of the $E1$ resonance. Finally, the information from the temperature-dependent resonant signal is used to shed light on the $4f$ and $5d$ magnetism in samarium.

The organization of the paper is as follows: Sec. II describes the sample and the experiment. The experimental results are presented in Sec. III. In Sec. IV, we consider the nonresonant contribution to the magnetic scattering, while Sec. V is devoted to the study of the resonance. We split the analysis of the resonant contribution into two sections, V A and V B, according to the physical nature of the intermediate levels in the resonant scattering process. In Sec. V A, we treat the $E2$ resonance of the localized $4f$ levels, focusing on

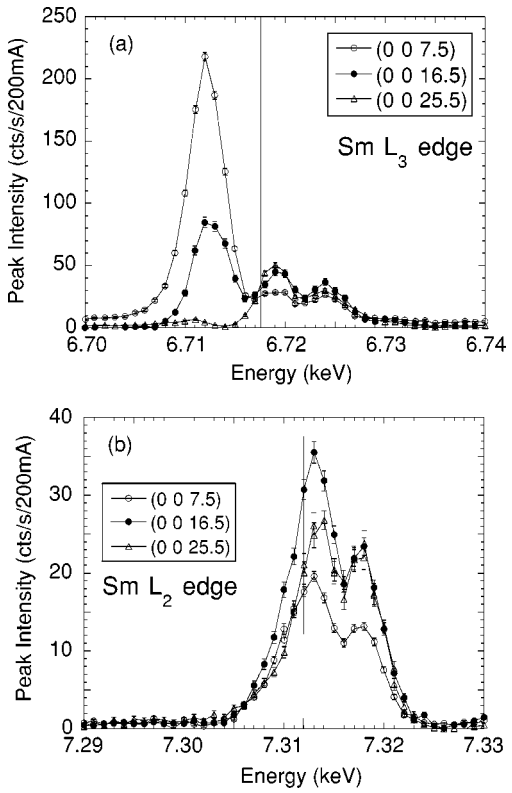

FIG. 1. Energy dependence of the measured peak intensity for several reflections from the hexagonal sublattice at the Sm L_3 edge (a) and L_2 edge (b). The solid lines are guides for the eye. The vertical line gives the position of the inflexion point in the fluorescence (taken from Ref. 9).

the information that may be derived from the angular dependence of the scattering cross section. In Sec. V B, the $E1$ transitions to the delocalized $5d$ states are considered and we introduce a phenomenological model to analyze RXMS data from antiferromagnetic materials with extended intermediate levels. The model is used in a self-consistent fashion to analyze the (resonant, nonmagnetic) white line in the fluorescence. In Sec. V C, the L_2 and L_3 data are brought together and a consistent analysis of the resonant line shapes of the white line and of the magnetic $E1$ and $E2$ contributions at both edges is given. In Sec. VI, we discuss the role of the $5d$ band in the long-range magnetic order in samarium. Finally, in Sec. VII, we present our conclusions.

II. SAMPLE AND EXPERIMENTS

An experimental difficulty in the study of rare-earth metals using x-ray scattering arises from the crystal quality. Single-crystal samples generally consist of an assembly of small crystallites with dimensions of the order of 0.1–0.5 mm. The mosaic spread of each crystallite can be as good as 0.02°, but the misorientations of neighboring crystallites can be as large as 0.5°. This feature, common to all rare earths, is pronounced in Sm, perhaps on account of the specific nine-plane compact stacking. A second problem is related to the surface quality of the sample. On account of the strong absorption at the $L_{2,3}$ edges, the presence of surface oxidation and ''dead magnetic layers''[29] or the surface roughness[30] complicate the line-shape analysis in a nontrivial manner. These material-related problems can be overcome by the use of epitaxial films prepared under UHV, with a thin protective cap layer deposited *in situ* to avoid oxidation once in air. Carefully monitored growth methods[31] lead to very homogeneous single-crystal films, with a mosaic spread of 0.1–0.3°.[32] A restriction is that the film has to be ''thick enough'' (typically several 1000 Å), so that the magnetic properties do not mainly reflect the effects of strains due to lattice mismatch at the substrate and capping interfaces. For these experiments, a 5000-Å-thick **c**-axis Sm film, with a 500-Å Nb protective cap has been used.[6,9,27] Preliminary x-ray scattering measurements at room temperature have shown that this film presents the ''Sm structure'' with a c parameter of 26.21 Å, similar to the bulk value. The coherence length of the Sm structure in the **c** direction is estimated to be of the order of 800 Å (30 unit cells). The full width at half maximum (FWHM) of rocking curves through the (0 0 9) and (0 0 18) charge Bragg reflections gives a mosaic spread of 0.13°.

To extract meaningful information from magnetic Bragg peak intensities requires an integral of the full scattered intensity. In neutron scattering or nonresonant x-ray magnetic diffraction this implies using sufficiently relaxed collimation and/or scanning some (angular) variable. Corrections for absorption, extinction, and instrumental resolution effects (Lorentz factor) may then be applied. Finally the data are refined towards a given magnetic structure taking into account the form of the geometric and polarization dependencies of the scattering amplitudes. In resonant x-ray magnetic diffraction experiments, when working close to an absorption edge one encounters, as an additional variable, the energy of excitation of the resonance: the resonant scattering amplitude depends strongly on the incident photon energy. In addition to the integration in reciprocal space one is now faced with integration (either explicit or implicit by use of relaxed monochromation) over the incident photon energy in order to collect full resonant intensities. The integration over energy is particularly delicate, as one needs to distinguish resonances related to different excitations. In this paper, the explicit incident photon energy dependence of angular integrated scans is used to deduce information on the polarized density of $4f$ and $5d$ states. Experimentally this requires a stable and well monochromated x-ray source, which may be tuned through the $L_{2,3}$ absorption edges. The intrinsic damping of the resonance amounts to 3.3 eV (FWHM) at the L_3 edge and 4.3 eV at the L_2 edge,[33] which demands an incident beam monochromaticity in the eV range at 7 keV. In addition, to separate the nonresonant, electric dipole and electric quadrupole resonant scattering it is necessary to use full polarization analysis of the incident and the scattered beam.

The experiments were carried out at the bending magnet beamline XMaS (BM28), the UK CRG beamline at the European Synchrotron Radiation Facility (France). A single toroidal mirror placed after the double Si (1 1 1) monochromator ensures the horizontal and the vertical focusing. The degree of linear polarization depends critically on the vertical opening of the primary slits before the monochromator. It

is 99.5% in the plane of the electron ring,[34] but degrades quickly with the vertical opening of the primary slits. Our compromise was a slits opening of 1.5 mm (vertical beam divergence 63 μrad), that cuts about $\frac{1}{2}$ of the photon flux, but gives a degree of linear polarization of 95%. The resulting calculated energy resolution is 1.7 eV at 6.72 keV (L_3 edge) and 1.9 eV at 7.31 keV (L_2 edge). The photon flux at the sample was of the order of 10^{11} photons/s at the maximum storage ring current of 200 mA.

The diffractometer was used in the four-circle geometry and equipped with a polarization analyzer on the detector arm. The sample was oriented with the (**a***,**c***) plane in the vertical scattering plane. A Cu (2 2 0) analyzer crystal, with a mosaic spread of 0.28° and a peak reflectivity of 3.5% at 6.7 keV was used for polarization analysis at the L_3 edge. At the L_2 edge, the analyzer was an Al (2 2 2) crystal with a measured mosaic spread of 0.13° and 4% peak reflectivity at 7 keV. If we use the linear (σ,π) polarizations as basis (i.e., polarizations perpendicular and parallel to the scattering plane, respectively), with incident σ polarization, as is the present case, charge Bragg reflections will only scatter into the σ polarization channel, whereas magnetic scattering (resonant and nonresonant) also scatters into the rotated σ-π channel. The Bragg angle of the polarization analyzer crystal being close to 45°, the charge background from the substrate is reduced by several orders of magnitude in the σ-π configuration. This configuration was used throughout all our measurements, mostly to benefit from the low background.

III. RESULTS

For the hexagonal sublattice at 50 K, the energy dependence was obtained at the L_3 edge by scanning along **c*** in wave-vector space at each incident energy. Three specular reflections (0 0 l), with $l=7.5$, 16.5, and 25.5, were studied. The integrated intensities, corrected for absorption using the method described in Ref. 22 and for the Lorentz factor,[35] are shown in Fig. 2(b), while Fig. 2(a) gives the energy dependence of the fluorescence, measured away from any Bragg position.

The linewidth in wave-vector space of the scans along **c*** does not show any variation with the incident photon energy [Fig. 2(d)] and the energy dependence of the resulting integrated intensity is identical to the energy scans at fixed wave-vector transfer shown in Fig. 1(a). This result enabled us to deduce the energy dependence of the L_3 resonance at three reflections from the cubic sublattice, (0.25 0 11.75), (0.25 0 15.25), and (0.25 0 18.25), at $T=8$ K, from the energy dependence of peak intensities. We measured scans along **c*** at only a few selected energies and obtained a linewidth that did not change with the energy. The energy dependence of ''integrated intensities'' was then estimated by multiplying the peak resonant intensities by the measured linewidth. The resulting integrated intensities have been corrected for the Lorentz factor and for the absorption and are shown in Fig. 2(c). They are approximately 1% of those measured at the same temperature for scattering from the hexagonal sites in the $E2$ channel and essentially of zero intensity at the position of the $E1$ resonance, except, perhaps, at the largest **Q** value. A quantitative analysis of the **Q** dependence of several magnetic reflections from both the hexagonal and the cubic sublattices, measured at 6.712 keV (Sec. V A 1) will confirm the quadrupolar character of this resonance.

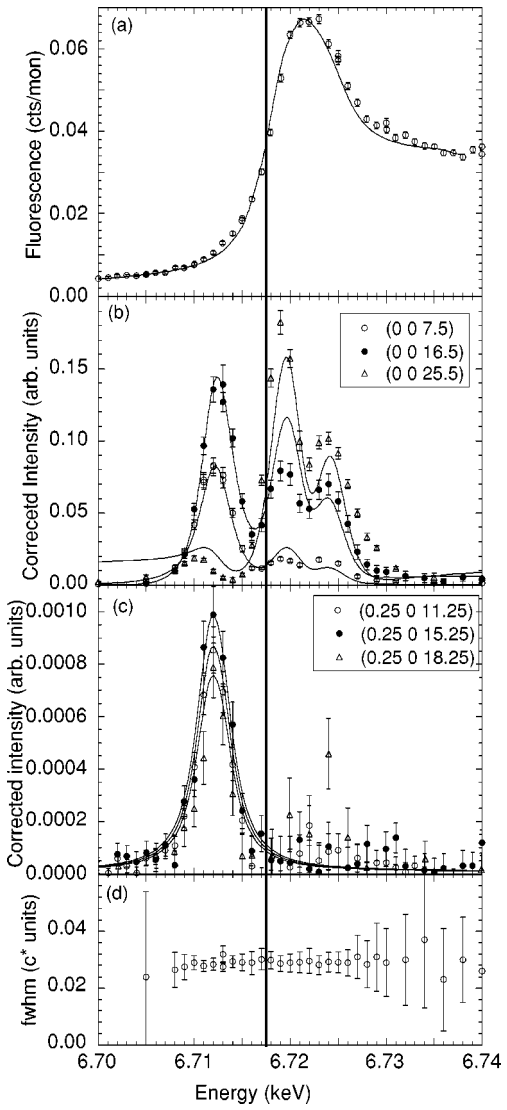

FIG. 2. Sm L_3 edge. Energy dependence of fluorescence (a), and of the integrated intensities of several reflections from the hexagonal sublattice (b) and the cubic sublattice (c). The linewidth of the scans along **c*** is constant as shown in (d) for the (0 0 16.5) reflection. The intensities have been corrected for absorption and for the Lorentz factor. The solid lines in (b) and (c) are the results of a calculation (Sec. V C). In (c), they show a simple Lorentzian line shape, with a FWHM $\Gamma=3.3$ eV, convoluted by an energy resolution of 1.7 eV, and scaled with the calculated polarization factors. The vertical line gives the position of the inflexion point in the fluorescence.

Similarly to the cubic sublattice reflections at the L_3 edge, the resonance associated with the hexagonal sublattice at the L_2 edge was obtained by measuring the linewidth along **c*** at a few energies and the energy dependence of peak intensities. The corrected ''integrated intensities'' are displayed in Fig. 3 with the measured fluorescence. For comparison with the L_3 data, the intensities have been scaled to the same

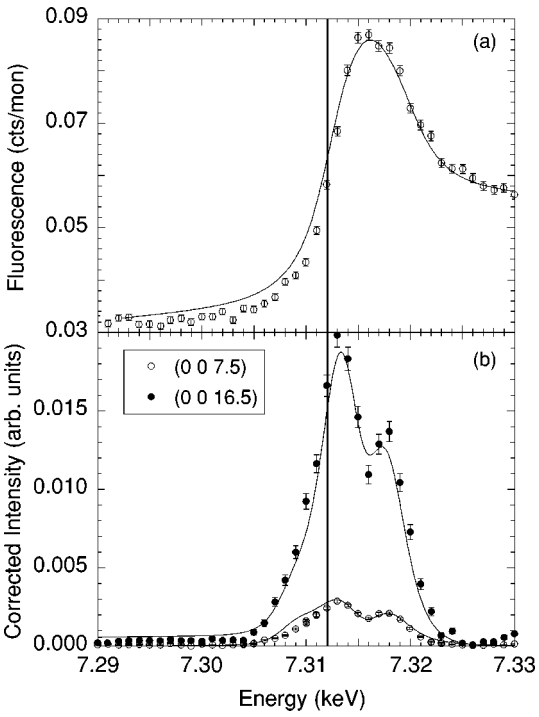

FIG. 3. Sm L_2 edge. Energy dependence of the fluorescence (a) and of the integrated intensities deduced from the measurement of peak intensities for several reflections from the hexagonal sublattice (b). The intensities have been corrected for absorption and for the Lorentz factor. The lines are the results of a calculation (Sec. V B). The vertical line gives the position of the inflexion point in the fluorescence.

incident photon flux, and corrected for the different analyzer reflectivities. Two main resonances are observed. They have the same **Q** dependence, similar to the $E1$ resonances at the L_3 edge, and their position with respect to the absorption edge is consistent with a dipole origin.[9] The substantial reduction of the $E2$ resonance at the L_2 edge has already been observed in other rare earths, in scattering[9,20,21] as well as in dichroism experiments.[36] Given the weakness of the measured signals, no study of the cubic sublattice was attempted at the L_2 edge.

IV. NONRESONANT MAGNETIC SCATTERING

At a given incident photon energy $\hbar\omega$, the integrated intensity, corrected for absorption and Lorentz factor, can be written as[10]

$$I = K_0 \left| \sum_{\text{atoms } j} e^{i\mathbf{Q}\cdot\mathbf{r}} [f_{\text{nonres}}(\mathbf{Q},\omega) + f_{E1}(\mathbf{k},\mathbf{k}',\omega) + f_{E2}(\mathbf{k},\mathbf{k}',\omega)] \right|^2 . \quad (1)$$

K_0 is a scale factor determined from charge scattering, and $\mathbf{Q}=\mathbf{k}-\mathbf{k}'$, where $\mathbf{k}$ ($\mathbf{k}'$) is the wave vector of the incident (scattered) radiation, and $\hbar\omega$ is the photon energy. $f_{\text{nonres}}(\mathbf{Q},\omega)$, $f_{E1}(\mathbf{k},\mathbf{k}',\omega)$, and $f_{E2}(\mathbf{k},\mathbf{k}',\omega)$ are the nonresonant, resonant dipole, and resonant quadrupole single-ion scattering amplitudes from atom j, respectively. The accurate determination of K_0 requires careful scaling of the intensities over 7–10 orders of magnitude, as described in more detail in Ref. 37. We will here content ourselves with reasonable orders of magnitude.

In the σ-π polarization channel studied here, the nonresonant amplitude is[38]

$$f_{\text{nonres}}(\mathbf{Q},\omega) = -ir_0 \frac{\hbar\omega}{m_e c^2} 2\sin^2\theta [(L_1+S_1)\cos\theta + S_3 \sin\theta]; \quad (2)$$

r_0 is the classical electron radius, θ is the Bragg angle, and L_1, S_1, and S_3 are projections of $L(\mathbf{Q})$ and $S(\mathbf{Q})$, which are the Fourier transforms of the effective orbital and spin magnetic moments: $L(\mathbf{Q})=(2-g_J)Jf_L(\mathbf{Q})$ and $S(\mathbf{Q})=(g_J-1)Jf_s(\mathbf{Q})$, g_J being the Landé factor.[39] The spin and orbital form factors, $f_s(\mathbf{Q})=\langle j_0\rangle$ and $f_L(\mathbf{Q})=\langle j_0\rangle+\langle j_2\rangle$, have been developed explicitly by Freeman and Desclaux and include the summation over all electrons.[40] The projections are along $\mathbf{u}_1$, $\mathbf{u}_2$, and $\mathbf{u}_3$, unit vectors in the directions of $\mathbf{k}+\mathbf{k}'$, $\mathbf{k}\times\mathbf{k}'$, and $\mathbf{k}-\mathbf{k}'$, respectively. In the present geometry, $L_1=L(\mathbf{Q})\sin\delta$, $S_1=S(\mathbf{Q})\sin\delta$, $S_3=-S(\mathbf{Q})\cos\delta$, where δ is the angle between **c** (assumed to be the positive direction of the spins) and $\mathbf{k}'-\mathbf{k}$. For specular reflections (0 0 l), the nonresonant contribution to the scattering amplitude reduces to

$$A_{\text{nonres}} = \sum_{\text{atoms } j} e^{i\mathbf{Q}\cdot\mathbf{r}_j} f_{\text{nonres}}(\mathbf{Q},\omega) = -F_M(\mathbf{Q}) ir_0 \frac{\hbar\omega}{m_e c^2} 2S(\mathbf{Q})\sin^3\theta. \quad (3)$$

$F_M(\mathbf{Q})$ is the magnetic structure factor. Assuming samarium to be in a pure Sm^{3+} state, and considering only the $4f$ contribution to the magnetism, $S(\mathbf{Q})=-\frac{25}{14}\langle j_0\rangle$. For the (0 0 7.5), (0 0 16.5), and (0 0 25.5) reflections, $F_M(\mathbf{Q})=-i\sqrt{3}$ and we obtain $A_{\text{nonres}}\approx 0.001r_0$, $0.004r_0$, and $0.007r_0$ respectively, at an incident photon energy of 6.7 keV (i.e., below the L_3 edge).

The intensity expected from these values can be estimated by comparing to the intensity measured at a charge Bragg reflection. We measured of the order of 10^7 photons/s in the σ-σ polarization channel at the (1 0 14) reflection from one structural domain, where the calculated charge structure factor is $59.3r_0$. Taking the geometrical corrections into account, we obtain an expected intensity $\approx$0.004 photon/s at (0 0 7.5). Such a low value is consistent with the fact that no nonresonant intensity was observed below the L_3 edge at this position. For the reflections at higher **Q**, the expected intensities are $\approx$0.04 photon/s at (0 0 16.5) and $\approx$0.05 photon/s at (0 0 25.5), which is about half the background level. We have not found unambiguous evidence for such intensity below the absorption edge with counting times of 60 s. The present calculation, however, neglects two effects: (i) the interference with the resonant amplitudes, and (ii) the $5d$ polarization. Calculations presented in Sec. V C suggest that the interference terms are non-negligible while, despite the pos-

sible importance of the $5d$ polarization,[4] we are able to ignore it on account of its compact form factor.

V. RESONANT MAGNETIC SCATTERING

The resonant amplitudes in x-ray scattering are usually expressed in the framework of an atomic model,[10] assuming that the intermediate states extend over a narrow band compared to the inverse lifetime of the core hole Γ. Based on the work by Hannon *et al.*,[10] Hamrick[41] and Hill and McMorrow[42] have developed some useful expressions for the scattering amplitudes. The formalisms differ slightly, and the correspondence is given in the Appendix. In the following, we will use the notations from Ref. 42.

The single-ion scattering amplitudes $f_{E1}(\mathbf{k},\mathbf{k}',\omega)$ and $f_{E2}(\mathbf{k},\mathbf{k}',\omega)$ [Eq. (1)] are written as matrix elements coupling the incident and scattered polarization vectors $\boldsymbol{\varepsilon}$ and $\boldsymbol{\varepsilon}'$:

$$f_{EL}(\mathbf{k},\mathbf{k}',\omega) = \frac{4\pi}{|\mathbf{k}|}\sum_{M=-L}^{L}[\boldsymbol{\varepsilon}'^{*}\cdot\mathbf{Y}_{LM}(\mathbf{k}')\mathbf{Y}_{LM}(\mathbf{k})\cdot\boldsymbol{\varepsilon}]F_{LM}(\omega). \quad (4)$$

$L=1$ or 2 for dipole or quadrupole respectively. $\mathbf{Y}_{LM}(\mathbf{k})$ are vector spherical harmonics. The factors $F_{LM}(\omega)$ reflect atomic properties, and determine the strength of the resonance:

$$F_{LM}(\omega)=\sum_{\alpha,\eta}\left|P(\alpha,\eta)\frac{\Gamma_{LM}(\alpha,\eta)/\Gamma}{(x-i)}\right|. \quad (5)$$

$x=(E_\eta-E_\alpha-\hbar\omega)/(\Gamma/2)$, where α is the initial (and final) state of the ion with energy E_α, and η is the intermediate excited state with energy E_η. $P(\alpha,\eta)$ represents the occupation and transition probabilities. $\Gamma_{LM}(\alpha,\eta)$ is the partial linewidth of the 2^L pole radiative decay, whereas Γ is the total width of the excited level, proportional to the inverse lifetime of the core hole.

The geometry of our experiment was chosen so as to keep the moments in the scattering plane. For the resonant processes we can write

$$f_{E1}(\mathbf{k},\mathbf{k}',\omega)=P_{E1}^{(1)}F_{E1}^{(1)}, \quad (6a)$$

$$f_{E2}(\mathbf{k},\mathbf{k}',\omega)=P_{E2}^{(1)}F_{E2}^{(1)}+P_{E2}^{(3)}F_{E2}^{(3)}. \quad (6b)$$

$F_{E1}^{(1)}$, $F_{E2}^{(1)}$, and $F_{E2}^{(3)}$ are amplitude factors, expressed as linear combinations of the $F_{LM}(\omega)$:

$$F_{E1}^{(1)}=\frac{3}{4|\mathbf{k}|}[F_{11}(\omega)\text{-}F_{1-1}(\omega)], \quad (7a)$$

$$F_{E2}^{(1)}=\frac{5}{4|\mathbf{k}|}[F_{22}(\omega)\text{-}F_{2-2}(\omega)], \quad (7b)$$

$$F_{E2}^{(3)}=\frac{5}{4|\mathbf{k}|}[F_{21}(\omega)\text{-}F_{2-1}(\omega)], \quad (7c)$$

$P_{E1}^{(1)}$, $P_{E2}^{(1)}$, and $P_{E2}^{(3)}$ are (geometrical) polarization factors determined by the characteristic directions of the experiment.[10,42] In the σ-π polarization channel and for collinear moments in the scattering plane,

$$P_{E1}^{(1)}=i\sin(\theta+\delta), \quad (8a)$$

$$P_{E2}^{(1)}=i\sin(\theta+\delta)[\cos(2\theta)+\sin(\theta+\delta)\sin(\theta-\delta)]. \quad (8b)$$

$$P_{E2}^{(3)}=i\cos[2(\theta+\delta)]\sin(\theta-\delta). \quad (8c)$$

A. Quadrupole resonance

1. L_3 edge

The $E2$ resonance has been most clearly observed at the L_3 edge. It involves highly localized $4f$ intermediate states and the atomic approximation appears to be justified since the energy width of the resonance is consistent with the theoretical value of Γ, 3.3 eV at the L_3 edge,[33] when the experimental energy resolution (1.7 eV) is taken into account. In this section, we confirm its quadrupole origin through the dependence on the wave-vector transfer.

The measured splitting between the $E1$ and $E2$ resonances is large and we can, in a first approximation, ignore the $E1$ contribution to the magnetic intensity at the energy of the $E2$ resonance. Similarly, the weak nonresonant contribution will be ignored in this section, as well as the interference terms. With these simplifications, the integrated intensity reduces to

$$I=K_0A(\mathbf{Q})|F_M(\mathbf{Q})(P_{E2}^{(1)}F_{E2}^{(1)}+P_{E2}^{(3)}F_{E2}^{(3)})|^2. \quad (9)$$

$A(\mathbf{Q})$ is the crystal volume fraction (domains): all magnetic domains contribute to the intensity at specular magnetic Bragg positions $(0\ 0\ l)$ (hexagonal sublattice), whereas nonspecular reflections (cubic or hexagonal) derive from a single pair of magnetic antiphase domains. The magnetic structure factor is $F_M(\mathbf{Q})=1$ for all cubic sublattice reflections and depends on $\mathbf{Q}$ for the hexagonal sublattice reflections (Table I). For one Sm^{3+} ion (five $4f$ electrons), atomic calculations lead to $F_{E2}^{(1)}\approx-0.074(r_0/2\lambda_{res})$ and $F_{E2}^{(3)}\approx F_{E2}^{(1)}/2$ (Appendix and Ref. 41), where λ_{res} is the photon wavelength at the resonant energy.

At the maximum of the $E2$ resonance, 6.712 keV, we performed L scans around the positions of nine ''hexagonal'' reflections (three specular and six nonspecular) and seven ''cubic'' reflections. The integrated intensities are summarized in Table I.

The intensity [Eq. (9)] can be written as a reduced intensity:

$$\tilde{I}=\frac{I}{A(\mathbf{Q})|F_M(\mathbf{Q})P_{E2}^{(1)}|^2}=K_0\left|1+\frac{p_{E2}^{(3)}}{P_{E2}^{(1)}}\frac{F_{E2}^{(3)}}{F_{E2}^{(1)}}\right|^2. \quad (10)$$

The reduced intensities $\tilde{I}$ are calculated assuming equal domain populations, and shown in Fig. 4 as a function of $P_{E2}^{(3)}/P_{E2}^{(1)}$. The solid line is a result of a least squares fit to the parabolic function, Eq. (10). The agreement is very good,

TABLE I. Integrated intensities at 8 K of several reflections from the hexagonal and the cubic sublattices, and applied corrections. μ^* is the absorption correction as defined in Ref. 22, A is the crystal volume fraction (domains), and the geometrical factors are those defined by Eqs. (8b) and (8c).

h	k	l	Integrated intensity	A	$F_M(\mathbf{Q})$	μ^* (mm^{-1})	Lorentz factor	$P_{E2}^{(1)}/i$	$P_{E2}^{(3)}/i$
0	0	16.5	0.353(12)	1	$-i\sqrt{3}$	1351	0.583	0.320	0.187
0	0	19.5	0.158(5)	1	$i\sqrt{3}$	1561	0.689	0.362	0.035
0	0	25.5	0.0084(6)	1	$-i\sqrt{3}$	1984	0.901	0.170	−0.562
1	0	14.5	0.206(13)	1/2	$2i\sin(5\pi/9)$	2437	0.147	0.070	0.839
1	0	15.5	0.015(4)	1/2	$2i\sin(\pi/9)$	2261	0.212	0.097	0.804
1	0	17.5	0.064(4)	1/2	$2i\sin(2\pi/9)$	2147	0.335	0.137	0.699
1	0	18.5	0.047(3)	1/2	$2i\sin(2\pi/9)$	2131	0.395	0.149	0.627
−1	0	14.5	0.094(6)	1/2	$2i\sin(5\pi/9)$	409	0.877	0.417	−0.079
−1	0	23.5	0.010(2)	1/2	$2i\sin(5\pi/9)$	1525	0.976	0.156	−0.619
0.25	0	8.75	0.058(5)	1/6	1	1532	0.118	0.101	0.487
0.25	0	9.25	0.011(2)	1/6	1	1456	0.147	0.125	0.485
0.25	0	11.75	0.0098(7)	1/6	1	1389	0.278	0.222	0.467
0.25	0	12.25	0.0120(7)	1/6	1	1398	0.302	0.238	0.461
0.25	0	15.25	0.0099(4)	1/6	1	1502	0.440	0.305	0.390
−0.25	0	8.75	0.090(5)	1/6	1	361	0.500	0.430	0.059
−0.25	0	9.25	0.012(1)	1/6	1	421	0.507	0.432	0.071

confirming the $E2$ character of this resonance. The position of the minimum of this parabola gives $F_{E2}^{(3)}/F_{E2}^{(1)}=0.51\pm0.01$, which is within the experimental error the expected value of 0.5 from atomic calculations.[41]

The reflections from the hexagonal sublattice originate from either both structural domains or one single structural domain. The fact that their corrected intensities fall on the same parabola confirms the assumption of equal population of the structural domains in this epitaxial film. Moreover, the reflections from the cubic sublattice, once normalized by the crystal volume fraction, also fall on the same curve. This is consistent with our assumption of the equal population of the magnetic domains. Importantly, these results indicate that the

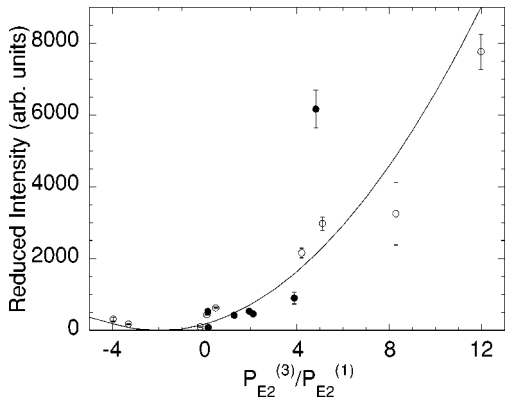

FIG. 4. Reduced intensities at 6.712 keV (L_3 quadrupole resonance), of several hexagonal (open circles) and cubic (full circles) reflections as a function of the reduced polarization factor $P_{E2}^{(3)}/P_{E2}^{(1)}$. The solid line is a fit to Eq. (10). Interference effects with the dipole resonance have been neglected but actually account for the small discrepancies observed for the weakest reflections (large error bars).

$4f$ polarization is, within experimental error, the same on the hexagonal and the cubic sites, i.e., independent of the local environment.

Turning now to the energy line shape, a simple analysis of the energy dependence of the $E2$ resonance is possible at the cubic sublattice reflections, where the $E1$ and the nonresonant contributions can be neglected. The solid lines in Fig. 2(c) result from a simultaneous fit of all reflections to the theoretical Lorentzian line shape of the $E2$ resonance (FWHM $\Gamma=3.3$ eV), convoluted by the instrumental energy resolution 1.7 eV. Using $F_{E2}^{(3)}/F_{E2}^{(1)}=0.5$ and a crystal fraction $\frac{1}{6}$ the only adjusted parameters are the scale factor and the energy of the resonance estimated at $E_{E2}=6.7121(2)$ keV. The agreement is good, allowing us to use the resonant energy E_{E2} as well as the theoretical linewidth in the interpretation of the resonant line shape at the hexagonal sublattice reflections (Sec. V C).

2. L_2 edge

At the L_2 edge, atomic calculations[41] give $F_{E2}^{(1)}\approx -0.054(r_0/2\lambda_{\mathrm{res}})$, and $F_{E2}^{(3)}\approx F_{E2}^{(1)}/2$, which leads to scattering amplitudes of the same order of magnitude as at the L_3 edge. However, no distinct quadrupole resonance is visible [Figs. 1(b) and 3]. At a qualitative level this discrepancy may be explained taking into account spin-orbit splitting of the $4f$ levels.[43] The L_3 edge will be dominated by transitions to the $j=\frac{7}{2}$ state while the L_2 edge connects the $j=\frac{5}{2}$. The $j=\frac{5}{2}$ are expected to lie lower in energy on account of the spin orbit splitting, and the five $4f$ electrons of Sm^{3+} will preferentially occupy these states. The number of vacant $j=\frac{5}{2}$ levels is hence reduced from 6 to 1, in contrast to the eight states available for the $j=\frac{7}{2}$ level. Crudely this will give a contribution to the intensity ratio $L_3/L_2=64/1$, which is consistent

with the apparent absence of quadrupole resonance at the L_2 edge and with the more detailed calculation presented in Sec. V C.

B. Dipole resonance: Model

In contrast with the $E2$ resonance, the $E1$ resonance involves $5d$ band magnetism. Indeed, the data show dipole resonances extending over some 10 eV, which demands adopting a somewhat different point of view from the isolated ion (atomic) standpoint.[10] As no $E1$ resonance was observed with sufficient intensity at positions corresponding to the long-range order in the cubic sublattice [Fig. 2(c)], this part of the analysis is restricted to magnetic intensities from the hexagonal sublattice, both at the L_2 and the L_3 edges.

Based on previous work,[18,28] we consider two issues: Sm is metallic and antiferromagnetic. First, on account of the metallic nature, it may be more appropriate to treat the empty $(5d)$ intermediate states of the $E1$ resonance as bands. The density of intermediate levels $D(E)$, available to the resonance, is determined by the site projected density of vacant states of the appropriate symmetry. For example, the $2p \rightarrow 5d \rightarrow 2p$ transition considered here requires the d (or $l=2$) projection. Second, antiferromagnetic ordering is represented by a spatial, rather than energetic, splitting of up and down spin density onto two magnetic sublattices, which defines a new Brillouin zone.

Before setting up an explicit model within which to evaluate the RXMS data, we note that electric dipole transitions are also responsible for the white line in the fluorescence. Hence a model for the energy line shape of the magnetic dipole resonance should be consistent with the observations on the energy line shape of the (nonmagnetic) white line. In this light, we develop a phenomenological picture with the constraint that one model density of effective intermediate states reproduces the white line and the energy profiles of the magnetic resonances at both the L_2 and the L_3 edges. In this paper, we content ourselves with such a consistent interpretation of the energy profiles. The decomposition of the effective density of levels to extract matrix elements and many body effects is not pursued. To our knowledge, the only existing quantitative analysis have been performed at the K edge of $3d$ elements where the data could more easily be related to simple models of spin orbit and exchange splitting.[44–46]

As an elementary model for the polarization on a given antiferromagnetic sublattice, we write the respective probability of finding the spin-up or spin-down lower level, as $0.5(1\pm p_l)$. The probability of finding an electron in this lower level is denoted a_l.[47] When necessary, to express differences in spin-up and spin-down radial matrix elements connecting the core and valence levels (breathing effect) a correction of the form $(1\pm\mu_l)$, can be made to the mean radial matrix element M_{5d}. While such corrections may, in some instances, play a vital role,[18,36] to simplify we will ignore them in the following analysis. Analogous quantities p_u, a_u, and μ_u are defined for the upper level. In general p_u is the negative of p_l. Note that in the ionic picture,[10] both exchange splitting and breathing were at first ignored, exchange splitting was then put in as a correction,[10,20] and then breathing was introduced.[36] In the following, the band splitting is assumed to be the same for all subbands of different orbital projection and the spin-orbit splitting of the intermediate levels and the spin splitting of the core levels are ignored.

The antiferromagnetic scattering amplitude at a given incident photon energy $h\omega$ is sensitive to resonant contributions integrated over the lower and upper bands, with density of states $D_l(E)$ and $D_u(E)$ and width W_l and W_u, respectively. Summing over both spin states, and assuming for simplification the same density of states for $M=1$ and $M=-1$, we obtain

$$F_{E1}\alpha\int_{E_l}^{E_l+W_l}\frac{M_{5d}B_lD_l(E-E_\alpha)}{\Gamma[x(E)-i]}dE + \int_{E_u}^{E_u+W_u}\frac{M_{5d}B_uD_u(E-E_\alpha)}{\Gamma[x(E)-i]}dE \tag{11}$$

with $B_l=p_l(1-a_l)$, $B_u=p_u(1-a_u)$ and $x(E)=(E-E_\alpha-\hbar\omega)/(\Gamma/2)$. E_l is the bottom of the lower energy band, which is split by the antiferromagnetic potential by an amount $2g$ from the lower edge of the upper band at E_u. As an explicit example, following the analysis of Hamrick,[41] we give the $E1$ contribution at the L_3 edge:

$$f_{E1}=r_0\left(\frac{1}{5}\right)(ka_0)^2M_{5d}m_ec^2\left(\frac{10}{18}\right)\left[\int_{E_l}^{E_l+W_l}dE\,\frac{B_lD_l(E-E_\alpha)}{\Gamma[x(E)-i]} + \int_{E_u}^{E_u+W_u}dE\,\frac{B_uD_u(E-E_\alpha)}{\Gamma[x(E)-i]}\right], \tag{12}$$

where a_0 is the Bohr radius. We note that the antiferromagnetic band model anticipates $f_{E1}^{L_3}=f_{E1}^{L_2}$. Substituting in the atomic radial matrix element[41] for an order of magnitude estimate together with a peak density of states $\simeq W^{-1}$ gives a peak intensity of

$$f_{E1}\approx r_0 0.36\,\mathrm{Pol}_{5d}P_{E1}^{(1)}, \tag{13a}$$

where Pol_{5d} is the effective polarization of the $5d$ band. An expression may be derived in a similar manner for the $E2$ scattering amplitude:

$$f_{E2}\approx r_0 0.12\,\mathrm{Pol}_{4f}(2P_{E2}^{(1)}+P_{E2}^{(1)}), \tag{13b}$$

where we have used the result that, for antiferromagnetic bands, $F_{E2}^{(1)}\approx 2F_{E2}^{(3)}$. In these estimates, $W_{5d}=10$ eV and $W_{4f}=0.5$ eV. Scaling to the charge scattering (Sec. III), one has $0.12r_0\approx 40$ cts/s at 200 mA ring current, this places the estimated amplitudes in reasonable accord with the measurements.

Now turning to the white line, we analyze it in a similar manner, but with coefficients $C_l=M_{5d}(1-a_l)$ and $C_u=M_{5d}(1-a_u)$, where we once again assume equal matrix elements for the upper and lower bands:

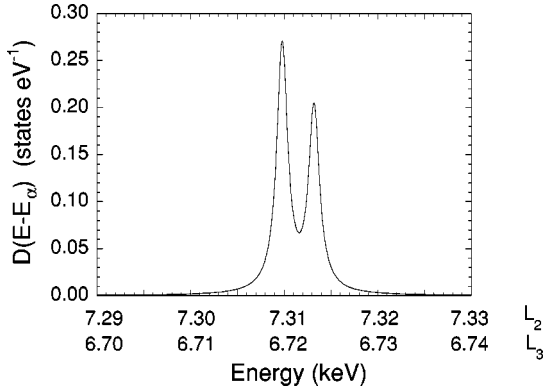

FIG. 5. 5*d* density of states used in the calculation of the energy line shape of the L_2 and L_3 resonances and of the fluorescence. This density of states is simply shifted by 590 eV between the L_2 and the L_3 edges.

$$f'' \alpha C_l \,\mathrm{Im}\left(\int_{E_l}^{E_l+W_l} \frac{D_l(E-E_\alpha)}{x(E)-i} \right) + C_u \,\mathrm{Im}\left(\int_{E_u}^{E_u+W_u} \frac{D_u(E-E_\alpha)}{x(E)-i} \right). \quad (14)$$

At the empirical level, the low-energy tail of the fluorescence spectra is expected to be dominated by, and hence may be used to estimate, the core hole lifetime. In the present case, it is consistent with the determination made from the study of the $E2$ resonance at the cubic sites. Given the core hole lifetime, the profile may be used to estimate $D(E-E_\alpha)$.

C. Analysis of the resonant line shape

The analysis of the resonant line shape has to include all contributions: nonresonant, $E1$, and $E2$. It has two parts: (i) the relative angular dependence of the spectra as one passes from one antiferromagnetic Bragg peak to another, given by the polarization factors, and (ii) the energy dependence of the scattering profiles. (i) is given by the relevant geometrical factors [Eqs. (8a)–(8c)]. The energy dependence (ii) of the $E1$ resonance at the L_2 edge is simpler than that of the L_3, since the $E2$ contribution is small, and is treated first.

Using the literature value of Γ, 4.3 eV at the L_2 edge,[32] a self-consistent loop of calculation has been made in which an initial $D(E)$ is selected and both the white line and antiferromagnetic response are calculated. The spectral weight function $D(E)$, Fig. 5, was iterated until consistency was obtained in the calculation of both the resonant magnetic and the white line data (Fig. 3). The model antiferromagnetic band splitting parameter g has been set to 1 eV. In this process g interacts (in practice only weakly) with $D(E)$. The exact value of g is not critical at this stage, but it cannot be claimed that a unique solution has been found. Help may come in the future from calculations of $D(E)$ by band-structure methods using the appropriate antiferromagnetic unit cell.

At the L_3 edge, comparison with the scattering data is more intricate on account of the significant $E2$ term. The shape and position of the $E2$ contribution has been taken from the observed scattering at the cubic sites (Sec. V A) and a nonresonant contribution (Sec. IV) has been introduced. The calculated $E2$ scattering amplitudes are $-0.046r_0$, $-0.061r_0$, and $+0.014r_0$ at (0 0 7.5), (0 0 16.5), and (0 0 25.5), respectively. Making allowance for the spin-orbit splitting of the $2p_{1/2}$ and $2p_{3/2}$ core levels, a rigid shift of 590 eV, the resonant line shape could then be calculated using the same density of states $D(E)$ as at the L_2 edge for the $E1$ scattering (solid lines in Fig. 2). The calculated white line at the L_3 edge likewise uses the same $D(E)$ and energy shift.

Finally, consistency was ensured by coming back to the L_2 edge with, this time, both a quadrupole and nonresonant contributions included. This gives the solid lines in Fig. 3. Once the model density of states $D(E)$ is chosen, only the ratio between $E1$ and $E2$ resonances and an overall scale factor need to be adjusted at each edge to obtain consistency over our full set of data. It is found that, while the $E1$ amplitude is essentially the same at both the L_2 and L_3 edges in agreement with the antiferromagnetic band model, the $E2$ contribution is approximately eight times weaker at the L_2 edge, as anticipated in a qualitative manner for transitions to spin-orbit split bands (Sec. V A 2). The only clear discrepancy in the global simulation is below the L_3 resonances at the highest **Q**, where the calculated profile is overestimated.

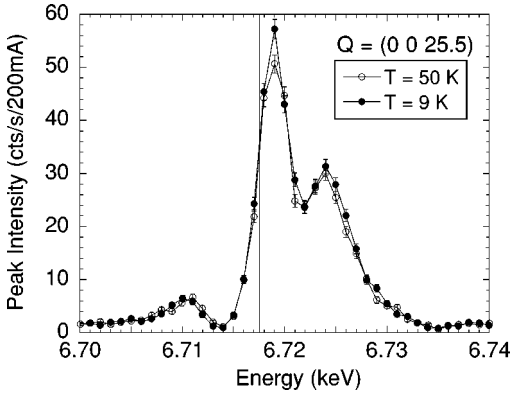

FIG. 6. Energy dependence of the (0 0 25.5) hexagonal sublattice reflection at 50 K (open circles) and at 9 K (full circles).

VI. 4*f* AND 5*d* MAGNETISM IN SAMARIUM

A neutron-diffraction experiment[4] has indicated that the moments on the hexagonal and the cubic sites are of equal amplitude. Our study of the $E2$ resonance in the low-temperature phase shows that the $4f$ polarization is independent of the local (hexagonal or cubic) environment, as might be expected from a pure rare earth where the $4f$ moments are localized and follow the Hund's rules. The question is more delicate when considering the $5d$ band. However, some light may be brought on the relative behaviors of the $4f$ and $5d$ polarizations by the study of the temperature dependence of the $E2$ and $E1$ resonances.

The energy line shape and the intensity of scattering from the hexagonal sites are not modified on cooling below $T_N{}^c$. This is shown for the (0 0 25.5) reflection at the L_3 edge in Fig. 6. The implication is that the establishment of long-

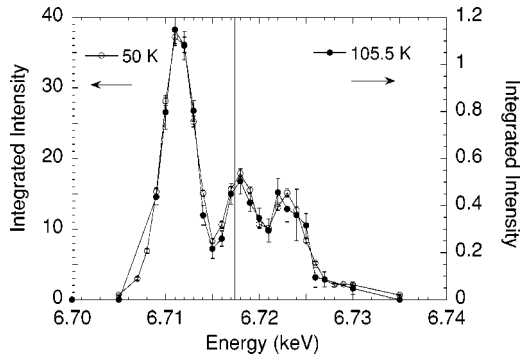

FIG. 7. Energy dependence of the (0 0 16.5) hexagonal sublattice reflection at 50 K (open circles) and at 105.5 K (full circles).

range magnetic order in the cubic sublattice does not measurably affect the projection of the $5d$ polarization on the hexagonal sites.

Moving to $T_N{}^h$, we investigated the magnetic polarization of the $4f$ and $5d$ states close to the transition. The energy dependence of the resonance at the (0 0 16.5) position measured at 105.5 K, close to $T_N{}^h$ is shown in Fig. 7. The intensities are 33 times smaller than at low temperature, but the energy line shape of the resonance is unchanged. The temperature dependence of the integrated intensity (scans along $\mathbf{c}^*$) has then been studied at two energies, 6.712 and 6.719 keV, chosen as representative of the $4f$ and the $5d$ resonances, respectively (Fig. 8). One sees that both the $E1$ and $E2$ resonances follow exactly the same temperature dependence. These results indicate that the $4f$ and $5d$ electrons are polarized with a constant ratio, even very close to $T_N{}^h$, as anticipated in a simple RKKY model.

No similar study could be performed for the cubic sublattice below $T_N{}^c$, due to the absence of observable $E1$ intensities. When allowance is made for the sample fraction observed at a given reflection (structural and magnetic domains) and for geometrical factors, assuming a $5d$ polarization parallel to the $4f$ polarization, the simple considerations presented in Sec. V fail to account for this absence.

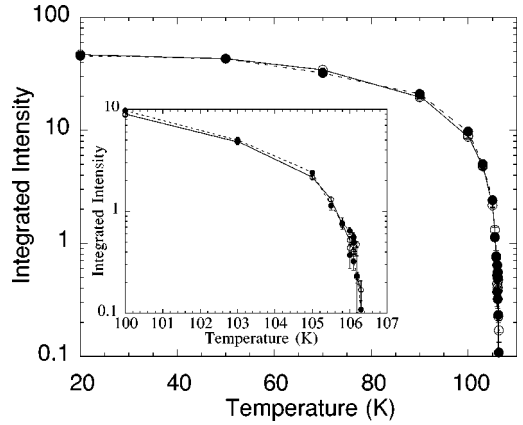

FIG. 8. Temperature dependence of (0 0 16.5) intensity at the dipole and quadrupole resonances, taken at 6.719 keV (full circles) and at 6.712 keV (open circles), respectively. The dipole intensities have been multiplied by 2.4 to allow easy comparison.

VII. CONCLUSION

This study of rare-earth magnetism by RXMS in molecular beam epitaxy grown films illustrates the use of sufficiently thick films to approach bulk material properties in much more favorable experimental conditions. The principal advantage of such films is the ability to prepare, in a controlled manner under conditions of ultrahigh vacuum, good quality, homogenous, monocrystalline samples with an inert protective layer. This, in particular, eliminates problems associated with surface degradation and oxidation, which have plagued experimental progress in this field.

Resonant magnetic scattering occurs for both the $4f$ (quadrupole) and the $5d$ (dipole) levels on the sites with local hexagonal symmetry and the ratio of $4f$ to $5d$ scattered intensity does not vary with the temperature. This is consistent with the idea of propagation of magnetic $4f$ order by itinerant $5d$ electronic states on the hexagonal sublattice. The scattered intensity from the hexagonal sites is, within the experimental resolution, identical at 8 and 50 K. This implies that neither the $4f$ nor the $5d$ polarization associated with the hexagonal sites is changed in a radical manner on passing below $T_N{}^c$, where the cubic sites order.

The situation is more complex for the cubic sublattice: on one hand the study of integrated intensities at the $E2$ $4f$ resonance suggests that the effective ordered magnetic moment in the $4f$ shell is likely to be similar in magnitude on the cubic and the hexagonal sites. On the other hand, $E1$ scattering is found exclusively at hexagonal sites. A simple interpretation in terms of negligible $5d$ polarization on the cubic sublattice is not satisfactory: if the cubic sites order independently from the hexagonal sublattice and given the large interplane separation in the cubic sublattice, ≈ 9 Å, the understanding of long-range magnetic order of the $4f$ moments becomes difficult. This point deserves further investigation.

The analysis of the energy dependence of the resonance focuses on the physical nature of the intermediate levels, the narrow-band character of the $4f$ level ($W \ll \Gamma$) contrasting with the broad, bandlike, $5d$ levels. Several features apparent in the data support this analysis. First, considering the $E1$ cross section as measured at the hexagonal sites, it proves possible to use *one* density of intermediate levels to model *both* the magnetic and the white line intensities at *both* the L_2 and the L_3 edges. The ratio $L_2/L_3 \simeq 1$, as anticipated in the model, and the absolute intensities are in order of magnitude agreement with the experiment. However, we fail to find a simple explanation for the lack of $E1$ resonance at the cubic sites. Passing to the $E2$ resonance, the antiferromagnetic model again, in the limit case $W \ll \Gamma$, consistently with the localized picture, yields agreement with the observed intensities and predicts $F_{E2}^{(1)} = 2F_{E2}^{(3)}$ as observed experimentally. Elementary considerations of the role of spin-orbit coupling shed some light on the marked absence of electric quadrupole scattering at the L_2 edge.

It is hoped that these results will encourage the use of RXMS in the study of microscopic magnetism in rare earths, with a new, more quantitative approach of the scattering am-

plitudes, and stimulate further study of this fascinating element.

ACKNOWLEDGMENTS

We acknowledge stimulating discussions with F. de Bergevin and M. Altarelli. Work at the XMaS beamline was supported by the EPSRC, United Kingdom.

APPENDIX

The following notes the relationship between two alternating forms of the resonant cross section, given by Hannon *et al.*,[10] and by Hamrick.[41] Hannon's formulation, further developed by Hill and McMorrow,[42] is widely used, but the relationship is useful if one wants to use the matrix elements calculated by Hamrick.

Starting from the coherent elastic magnetic scattering cross section[48] the multipole expansion performed by Hannon *et al.* and by Hamrick lead to the resonant single-ion amplitude, Eqs. (A1) and (A2), respectively,

$$f_{EL}(\mathbf{k},\mathbf{k}',\omega) = \frac{4\pi}{|\mathbf{k}|}\sum_{M=-L}^{L}[\boldsymbol{\varepsilon}'^{*}\cdot\mathbf{Y}_{LM}(\mathbf{k}')\mathbf{Y}_{LM}(\mathbf{k})\cdot\boldsymbol{\varepsilon}]F_{LM}(\omega), \quad \text{(A1)}$$

$$f_{EL}(\mathbf{k},\mathbf{k}',\omega) = \frac{E_\eta - E_\alpha}{\hbar\omega}\frac{r_0}{x-i}\sum_{M=-L}^{L}A_{LM}(\omega)P_{LM}(\omega), \quad \text{(A2)}$$

with $x=(E_\eta - E_\alpha - \hbar\omega)/(\Gamma/2)$. The correspondence between Eqs. (A1) and (A2) is simply

$$\frac{E_\eta - E_\alpha}{\hbar\omega}\frac{r_0}{x-i}A_{LM}(\omega) = \frac{4\pi}{|\mathbf{k}|}F_{LM}(\omega). \quad \text{(A3)}$$

In both references, the above relations are then expressed in a different, but equivalent, formalism, where the unit polarization direction **z** at the atomic sites appears explicitly, which is more convenient in the interpretation of scattering data. The developments to the different orders in **z** lead respectively to Eqs. (A4) (Hannon) and (A5) (Hamrick):

$$f_{EL}(\mathbf{k},\mathbf{k}',\omega) = \frac{4\pi}{|\mathbf{k}|}\sum_{n=0}^{2L}F_{EL}^{(n)}P_{EL}^{(n)}, \quad \text{(A4)}$$

$$f_{EL}(\mathbf{k},\mathbf{k}',\omega) = \frac{E_\eta - E_\alpha}{\hbar\omega}\frac{r_0}{x-i}\sum_{n=0}^{2L}\tilde{A}_n^{(EL)}\tilde{P}_n^{(EL)}. \quad \text{(A5)}$$

Hill and McMorrow give the relationship between the $F_{EL}^{(n)}$ and $F_{LM}(\omega)$,[41] and Hamrick writes the correspondence between the polarization factors $\tilde{P}_n^{(EL)}$ from Eq. (A5) and the $P_{LM}(\omega)$ from Eq. (A3). Simple algebra then leads to

$$F_{E1}^{(n)} = \frac{1}{2\lambda_{\rm res}}\frac{r_0}{x-i}\tilde{A}_n^{(E1)}, \quad n=0,\ 1,\ 2, \quad \text{(A6a)}$$

$$F_{E2}^{(n)} = \frac{1}{2\lambda_{\rm res}}\frac{r_0}{x-i}\tilde{A}_n^{(E2)}, \quad n=0,\ 4, \quad \text{(A6b)}$$

$$F_{E2}^{(1)} = \frac{1}{2\lambda_{\rm res}}\frac{r_0}{x-i}(2\tilde{A}_1^{(E2)}), \quad \text{(A6c)}$$

$$F_{E2}^{(2)} = \frac{1}{2\lambda_{\rm res}}\frac{r_0}{x-i}(\tilde{A}_0^{(E2)} + \tilde{A}_2^{(E2)}), \quad \text{(A6d)}$$

$$F_{E2}^{(3)} = \frac{1}{2\lambda_{\rm res}}\frac{r_0}{x-i}(\tilde{A}_1^{(E2)} + \tilde{A}_3^{(E2)}), \quad \text{(A6e)}$$

where $\lambda_{\rm res}$ is the photon wavelength at the resonant energy.

*Permanent address: European Synchrotron Radiation Facility, BP 220, F-38043 Grenoble Cedex, France.

[1] A. H. Daane, R. E. Rundle, H. G. Smith, and F. H. Spedding, Acta Crystallogr. **7**, 532 (1954).

[2] E. M. Forgan (private communication).

[3] J. M. Lock, Proc. Phys. Soc. London, Sect. B **70**, 566 (1957); K. A. McEwen, P. F. Touborg, G. J. Cock, and L. W. Roeland, J. Phys. F: Met. Phys. **4**, 2264 (1974).

[4] W. C. Koehler and R. M. Moon, Phys. Rev. Lett. **29**, 1468 (1972).

[5] S. L. Lee, E. M. Forgan, S. J. Shaikh, C. C. Tang, W. G. Strirling, S. Langridge, A. J. Rollason, M. M. R. Costa, M. J. Cooper, E. Zukowski, J. B. Forsyth, and D. Fort, J. Magn. Magn. Mater. **127**, 145 (1993).

[6] K. Dumesnil, C. Dufour, Ph. Mangin, M. Hennion, and P. J. Brown, Phys. Rev. B **60**, 10 743 (1999).

[7] N. W. Ashcroft and N. D. Mermin, *Solid State Physics* (Saunders College Publishing, Harcourt Brace College Publishers, Fort Worth, TX, 1976).

[8] W. Marshall and S. W. Lovesey, *Theory of Thermal Neutron Scattering* (Oxford University Press, Oxford, 1971).

[9] A. Stunault, C. Vettier, N. Bernhoeft, F. de Bergevin, C. Dufour, and K. Dumesnil, Proc. SPIE **3773**, 295 (1999).

[10] J. P. Hannon, G. T. Trammell, M. Blume, and D. Gibbs, Phys. Rev. Lett. **61**, 1245 (1988); the authors then introduced the exchange splitting as a correction: *ibid.* **62**, 2644 (1989).

[11] J. P. Hill, D. F. McMorrow, A. T. Boothroyd, A. Stunault, C. Vettier, L. E. Berman, M. v. Zimmermann, and Th. Wolf, Phys. Rev. B **61**, 1251 (2000).

[12] D. B. Pengra, N. B. Thoft, M. Wulff, R. Feidenhans'l, and J. Bohr, J. Phys.: Condens. Matter **6**, 2409 (1994).

[13] A. Stunault, C. Vettier, F. de Bergevin, F. Maier, G. Grübel, R. M. Galéra, and S. B. Palmer, J. Magn. Magn. Mater. **140–144**, 753 (1995).

[14] B. A. Everitt, M. B. Salamon, B. J. Park, C. P. Flynn, T. Thurston, and D. Gibbs, Phys. Rev. Lett. **75**, 3182 (1995).

[15] A. Vigliante, M. J. Christensen, J. P. Hill, G. Helgesen, S. Aa. Sørensen, D. F. McMorrow, D. Gibbs, R. C. C. Ward, and M. R. Wells, Phys. Rev. B **57**, 5941 (1998).

[16] E. Lidström, D. Mannix, A. Hiess, J. Rebizant, F. Wastin, G. H. Lander, I. Marri, P. Carra, C. Vettier, and M. J. Longfield, Phys. Rev. B **61**, 1375 (2000).

[17] J. P. Goff, R. S. Sarthour, D. F. McMorrow, F. Yakhou, A. Stunault, A. Vigliante, R. C. C. Ward, and M. R. Wells, J. Phys.: Condens. Matter **11**, L139 (1999).

[18] S. Langridge, J. A. Paixão, N. Bernhoeft, C. Vettier, G. H. Lander, D. Gibbs, S. Aa. Sørensen, A. Stunault, D. Wermeille, and E. Talik, Phys. Rev. Lett. **82**, 2187 (1999).

[19] A. Stunault, C. Vettier, F. de Bergevin, N. Bernhoeft, V. Fernandez, S. Langridge, E. Lidström, E. J. Lorenzo-Diaz, D. Wermeille, L. Chabert, and R. Chagnon, J. Synchrotron Radiat. **5**, 1010 (1998); S. D. Brown, P. Thompson, M. J. Cooper, J. Kervin, D. F. Paul, W. G. Stirling, and A. Stunault, Nucl. Instrum. Methods Phys. Res. A **467–468**, 727 (2001).

[20] Doon Gibbs, D. R. Harshman, E. D. Isaacs, D. B. McWhan, D. Mills, and C. Vettier, Phys. Rev. Lett. **61**, 1241 (1988); Doon Gibbs, G. Grübel, D. R. Harshman, E. D. Isaacs, D. B. McWhan, D. Mills, and C. Vettier, Phys. Rev. B **43**, 5663 (1991).

[21] S. C. Perry, M. M. R. Costa, W. G. Stirling, M. J. Longfield, D. Mannix, and T. Brückel, J. Phys.: Condens. Matter **10**, 1951 (1998).

[22] K. Dumesnil, A. Stunault, Ph. Mangin, C. Vettier, D. Wermeille, N. Bernhoeft, S. Langridge, C. Dufour, and G. Marchal, Phys. Rev. B **58**, 3172 (1998).

[23] J. Bohr, D. Gibbs, and K. Huang, Phys. Rev. B **42**, 4322 (1990).

[24] M. K. Sanyal, D. Gibbs, and M. Wulff, Phys. Rev. B **49**, 1079 (1994).

[25] D. Watson, E. M. Forgan, W. J. Nuttall, W. G. Stirling, and D. Fort, Phys. Rev. B **53**, 726 (1996); D. Watson, W. J. Nuttall, E. M. Forgan, S. C. Perry, and D. Fort, *ibid.* **57**, R8095 (1998).

[26] D. Watson, E. M. Forgan, W. G. Stirling, W. J. Nuttall, S. C. Perry, M. M. R. Costa, and D. Fort, J. Magn. Magn. Mater. **140–144**, 743 (1995).

[27] K. Dumesnil, C. Dufour, A. Stunault, and Ph. Mangin, J. Phys.: Condens. Matter **12**, 3091 (2000).

[28] N. Bernhoeft, J. Alloys Compd. **303–304**, 472 (2000).

[29] D. Wermeille, Ph.D. thesis, Ecole Polytechnique de Lausanne, 1998; N. Bernhoeft, Acta Crystallogr., Sect. A: Found. Crystallogr. **55**, 274 (1999).

[30] R. M. Osgood, III, S. K. Sinha, J. W. Freeland, Y. U. Iderza, and S. D. Bader, J. Appl. Phys. **85**, 4619 (1999).

[31] J. Kwo, M. Hong, and S. Nakahara, Appl. Phys. Lett. **46**, 319 (1986).

[32] R. A. Cowley, in *Dynamical Properties of Unconventional Magnetic Systems*, Vol. 349 of *NATO Science Series E*, edited by A. T. Skjeltorp and D. Sherrington (Klewer, New York, 1998).

[33] W. Bambinek, B. Crasemann, R. W. Fink, H. U. Freund, H. Mark, C. D. Swift, R. E. Price, and P. Venugopala Rao, Rev. Mod. Phys. **44**, 716 (1972).

[34] D. Laundy (private communication). This value is the present value with the whole storage ring tuned to low beta. In an earlier mode, consisting of alternating low beta and high beta sections, the polarization on orbit was 99.8%, as shown in D. Laundy, S. Brown, M. J. Cooper, D. Bowyer, P. Thompson, D. F. Paul, and W. G. Stirling, J. Synchrotron Radiat. **5**, 1235 (1998).

[35] The Lorentz correction for a **Q** scan within the $(\mathbf{k},\mathbf{k}')$ plane is $I\alpha ff^*/\sin(\theta+\delta)$, where θ is the Bragg angle and δ is the angle between **Q** and the direction of the scan, as detailed, for example, in B. Lebech, in *Magnetic Neutron Diffraction*, edited by A. Furrer (World Scientific, Singapore, 1993), p. 58. This is straightforward for longitudinal scans ($\delta=0$). For scans in a different direction, care should be taken when affecting the proper sign to δ.

[36] M. van Veenendaal, J. B. Goedkoop, and B. T. Thole, Phys. Rev. Lett. **78**, 1162 (1997), and references therein.

[37] V. Fernandez, C. Vettier, F. de Bergevin, C. Giles, and W. Neubeck, Phys. Rev. B **57**, 7870 (1998).

[38] M. Blume and D. Gibbs, Phys. Rev. B **37**, 1779 (1988).

[39] J. Jensen and A. R. Mackintosh, *Rare Earth Magnetism—Structures and Excitations* (Clarendon, Oxford, 1991).

[40] A. J. Freeman and J. P. Desclaux, J. Magn. Magn. Mater. **12**, 11 (1979).

[41] M. D. Hamrick, Ph.D. thesis, Rice University, Houston, Texas, 1994.

[42] J. P. Hill and D. F. McMorrow, Acta Crystallogr., Sect. A: Found. Crystallogr. **A52**, 236 (1996).

[43] M. S. S. Brooks and B. Johansson, in *Handbook of Magnetic Materials*, edited by K. H. J. Buschow (Elsevier, New York, 1993), Vol. 7, Chap. 3.

[44] A. Stunault, F. de Bergevin, D. Wermeille, C. Vettier, T. Brückel, N. Bernhoeft, G. J. McIntyre, and J. Y. Henry, Phys. Rev. B **60**, 10 170 (1999).

[45] W. Neubeck, C. Vettier, F. de Bergevin, F. Yakhou, D. Mannix, O. Bengone, M. Alouani, and A. Barbier, Phys. Rev. B **63**, 134430 (2001).

[46] Jun-ichi Igarashi and Manabu Takahashi, Phys. Rev. B **63**, 184430 (2001).

[47] Since the model contains no exchange splitting, the probability to find either a spin up or a spin down quasiparticle in a given band is the same. The Fermi functions are the same. The probability is taken independent of the orbital projection; this ensures zero orbital angular momentum. Where necessary (e.g., in insulators) this constraint may be relaxed.

[48] M. Blume, J. Appl. Phys. **57**, 3615 (1985); in *Resonant Anomalous Scattering, Theory and Applications*, edited by G. Materlik, C. J. Sparks, and K. Fischer (North-Holland, Amsterdam, 1994), p. 495.